https://doi.org/10.1016/j.ijmecsci.2019.105097 **This is the Pre-Published Version.**

Microstructural Material Characterization of Hypervelocity-impact-induced Pitting Damage

Wuxiong CAO[a,b‡], Yafeng WANG[b‡], Pengyu ZHOU[b‡], Xiongbin YANG[b‡], Kai WANG[b], Baojun PANG[a], Runqiang CHI[a] and Zhongqing SU[b,c*]

[a] School of Astronautics
Harbin Institute of Technology, Harbin 150080, P.R. China

[b] Department of Mechanical Engineering
The Hong Kong Polytechnic University, Kowloon, Hong Kong SAR

[c] The Hong Kong Polytechnic University Shenzhen Research Institute
Shenzhen 518057, P.R. China

Submitted to *International Journal of Mechanical Sciences*

(initially submitted on 27th June 2019; revised and re-submitted on 14 August 2019)

‡ PhD student

* To whom correspondence should be addressed. Tel.: +852-2766-7818, Fax: +852-2365-4703;
Email: Zhongqing.Su@polyu.edu.hk (Prof. Zhongqing SU, *Ph.D.*);

Abstract

In a hypervelocity impact (HVI) between the micrometeoroids/orbital debris (MMOD) and multi-layered shielding mechanisms of spacecraft, the debris cloud, formed by shattered materials of the outer bumper layer and projectile, commits multitudinous pitting craters and cracks that are disorderedly scattered in the rear wall layer. Material degradation due to the pitting damage is a precursor of structural fragmentation and system failure of the space assets. In this study, microscopic material degradation of the rear wall of a typical dual-layered Whipple shield, initiated and intensified by the debris cloud-engendered pitting damage, is characterized using metallographic analysis including optical microscope (OM), laser scanning microscope (LSM), scanning electron microscope (SEM) and X-ray diffraction (XRD). Results have revealed that 1) the degree of material degradation shows difference in the central cratered area, the ring cratered area, and the spray area, respectively; 2) the dynamic recrystallization gives rise to the formation of fine grains adjacent to pitting craters; 3) the extents of recrystallization and dislocation depend on the strain rate levels during HVI; and 4) the temperature elevation, caused by the heat transformed from the adiabatic plastic deformation energy and shock heating, warrants the recrystallization. Two types of damage, namely micro-voids and micro-cracks, are identified beneath the pitting damage area; under the extremely high compressive strain rate induced by HVI, micro-voids are initiated by the nucleation of grains or deteriorate from existing material defects, and these micro-voids further expand at the grain boundaries and within the grains to form micro-cracks under a tensile-type wave converted from the HVI-induced shock wave.

***Keywords*:** HVI; microstructural material characterization; debris cloud; pitting damage; dynamic recrystallization

1. Introduction

Amongst countless MMOD that are cluttering in low Earth orbit (LEO), over 23,000 of them are larger than 5 cm and traceable, which are mingled with another ~750,000 colloquially called "*flying bullets*" sized between 1~5 cm. MMOD smaller than 1 cm are estimated to be ~170 million. MMOD are flying around Earth at speeds over 7.9 km/s (*i.e.*, the first cosmic velocity) [1,2]. The untraceable MMOD have posed a potential threat of HVI (a scenario with an impact velocity exceeding 3 km/s) to orbiting spacecraft (*e.g.*, satellites, space stations, shuttles), and jeopardized their operational safety and structural integrity [3].

In general, the average HVI speed can vary from 2 to 19 km/s (double the first cosmic velocity) in LEO [4], and at such a velocity, the strength of the object material is sufficiently small compared to its inertial force [5].To minimize HVI hazard to orbiting spacecraft, a variety of shielding mechanisms have been designed and installed on spacecraft, as typified by Whipple shields including stuffed Whipple shields and multi-wall Whipple shields [6]. Such multi-layered Whipple shields can, in most circumstances, protect the shell structure of spacecraft from HVI attacks when the MMOD are smaller than 1 cm in size. An untraceable MMOD beyond 1 cm possibly penetrates the outer bumper layer and multi-layered insulation (MLI), and upon penetration, the MMOD fragmentations, together with shattered materials of bumper layer and MLI, form a debris cloud that subsequently impinges the inner rear wall layer (or shell structure of spacecraft), leading to multitudinous, disorderedly scattered pitting craters and cracks in the rear wall or even direct penetration.

Depending on the sizes and velocities of MMOD, as well as shielding configuration, debris cloud-induced damage in rear wall layer usually manifests itself with a high degree of complexity, which can be broadly classified as macro-damage (*e.g.*, craters, cracks, spalls, penetrated holes, *etc.*) and micro-damage (*e.g.*, dimples, micro-voids, micro-cracks, dislocations, *etc.*) [7-15]. The macro-damage can be detected and assessed with mature methods such as gas leakage detection, camera-based surface inspection, on-orbit acoustic emission, *etc.* [3]. Nevertheless, these prevailing detection methods are unwieldy to pinpoint and evaluate micro-damage, which, however under repetitious loads, expediate material degradation and deterioration. The material degradation, though initially at an unperceivable scale, can later compromise structural integrity and performance, leading to fragmentation and even failure of the entire spacecraft without timely detection and follow-up remedial measures.

It is thus of vital importance to advance the understanding of HVI-engendered material degradation and debris cloud-generated damage in the rear wall layers. Relevant researches have received a great deal of attention since the launch of Sputnik-1 in the 1950s including (1) cratering, spallation and microstructure changes in thick targets; (2) perforation and hole formation in thin, single thickness targets; (3) crater distribution on the rear wall of Whipple shields, *etc.*[16-19]. Representatively, Murr *et al.* [8] examined the damage in 6061-T6 alloy under HVI when the impact velocities were in a range from 1.7 to 5.2 km/s, and observed micro-bands beneath the crater periphery and near the crater bottom. Zhen *et al.* [9] interrogated material properties of Al-6Mg alloy under HVI when the impact speeds were 1 km/s and 3.2 km/s, respectively, to unveil micro-voids, micro-cracks, shear localization, and adiabatic shear bands (ASB) in the region near the crater bottom, as well as the dynamic recrystallization adjacent to the crater bottom. Focusing on 2519-T87 alloy under an oblique impact with an impact speed of 0.816 km/s, Liang *et al.* [10] confirmed that ASB and micro-bands were formed around the craters, and the microhardness presents different extents at the entering, stable-running and leaving stages. Zou *et al.* [11,12] argued that the deformed microstructure beneath the craters in AM60B alloy under HVI could be classified into three zones when the impact was 4 km/s, namely dynamic recrystallization zone, high density deformation twining zone, and low-density deformation twining zone; while when the speed increased to 5 km/s, four zones (*i.e.*, ultrafine grain zone, ultrafine grain and deformation twining zone, high-density deformation twining zone, and low-density deformation twining zone) were noted. In addition, equiaxed refined recrystallization grains were captured in the region adjacent to the craters formed by twining-induced dynamic recrystallization.

Nevertheless, majority of existing studies have been accomplished with an aim to characterize the change in material properties of a single layer of thick plate (tens of millimeters) under HVI from a single projectile that is larger than 1 mm in diameter, with various impact velocities and incident angles being the key parameters to be considered. In contrast, in-depth insight into the pitting damage and material degradation of the rear wall layer engendered by a debris cloud that is formed by the shattered material of the projectile and outer bumper layer – a two-layered shielding structure, has yet been well explored. In practice, most space structures feature multi-layered bumpers, penetration of any of which by a single projectile is likely to create a debris cloud consisting of numerous shattered projectiles sized between 10 and 100 μm. Consequently, a debris cloud impacts the rear wall (usually ~3.5 mm in thickness) and generates pitting damage scattered disorderedly over a wide area [20,21]. High temperature, high pressure and high deforming material strain rates ($\sim 10^6 \sim 10^8$ s^{-1}) are induced along with the debris cloud [5,9,12], and as a consequence the material manifests complicated and unique properties that are significantly distinct from those under the impact of a single projectile.

In recognition of the lack of the research effort in interrogating material degradation of multi-layered shielding structures under debris cloud-induced HVI, microstructural material characterization is performed in this study using a typical dual-layered Whipple shield made of 5A06 aluminium alloy, when the shield undergone HVIs up to 6 km/s. It is noteworthy that different from the material characterization under a quasi-static or dynamic load in which the progress of material change can be followed in a timely manner, the trace of structural response to a transient HVI is a daunting task, because the deformation and fracture of the target complete in a momentary duration of micro-second, and the initial shock stress rising and temperature fluctuation take place even within several nano-seconds. All these have imposed a challenge on material characterization for Whipple shields under debris cloud-induced HVI. Considering the fact that the different stages of material degradation initiated by HVI-induced damage in the rear wall layer are closely related to the physical process of micro-voids nucleation and expansion, the material characterization in this study features a twofold emphasis: 1) the pitting damage in the rear wall layer induced by the debris cloud is delineated, and 2) the microstructural changes, including formation and growth of micro-voids, in different pitting damage areas are quantified, which can be used to reflect the different stages of material degradation throughout a HVI process.

2. Material Selection and HVI Experiment Set-up

A typical dual-layered Whipple shield, as the impact target, is designed and fabricated, as displayed schematically in Fig. 1(a). The shield consists of a bumper layer (6061-T1 alloy, 1 mm thick) and a rear wall layer (5A06 aluminium alloy, 3 mm thick) with a shield spacing of 100 mm. Both layers have a planar dimension of 300 mm × 300 mm. 5A06 alloy, with the key chemical compositions (wt.%) of 5.8~6.8% Mg, 0.4% Fe, 0.02~0.1% Ti, 0.4% Si, 0.5~0.8% Mn, 0.1% Cu, 0.2% Zn, and balance Al. Most of the grain sizes are in a range from 30 to 70 μm, and the average size is about 40 μm (see Fig. 2).

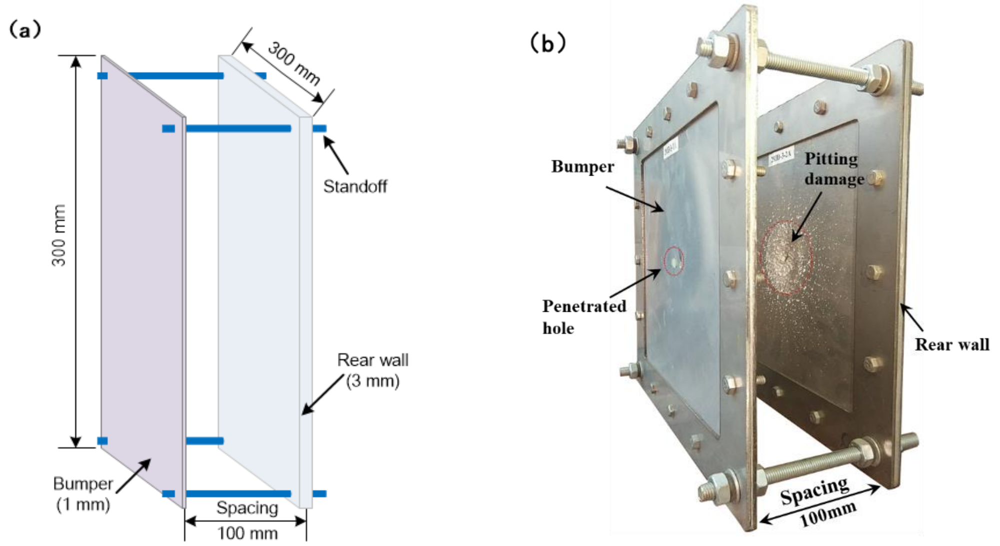

Fig. 1. (a) Schematic of the dual-layered Whipple shield fabricated for HVI test; and (b) photograph of the Whipple shield after HVI test.

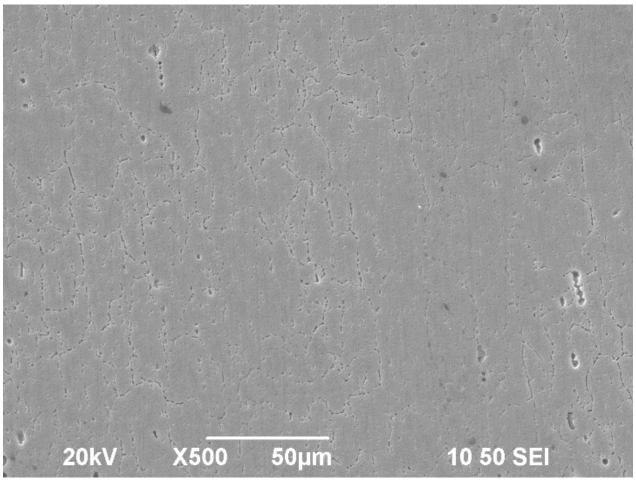

Fig. 2. SEM (JEOL JSM-6490) image of the base metal 5A06 alloy.

HVI tests are planned and carried out at Harbin Institute of Technology, China, using a two-stage light gas gun. In each test, a spherical aluminium projectile (AL-2017, Ø 3.2 mm or 4.5 mm) is launched via the light gas gun and normally impact the dual-layered Whipple shield. The selected impact speed, in a range from 4.13 to 5.93 km/s, is sufficient to generate instant kinetic energy and drive the projectile to penetrate the bumper layer. Upon penetration, debris cloud is created, mainly comprising shattered particles and jetted portion of the bumper layer, and the cloud further impinges the rear wall layer, leaving pitting damage with hundreds of clustered, localized craters and cracks that are scattered disorderedly over a wide area, as observed in Fig. 1(b).

3. Characterization of Rear Wall Layer

3.1. Structural Features of Debris Cloud

It is first of necessity to shed light on the structural characteristics of HVI-engendered debris cloud including its mass and velocity distribution, to which the pattern of damage in the rear wall layer is closely associated. The formation and expansion of debris cloud is captured by a flash X-ray radiography system (Scandiflash Model XT-150) that consists of four X-ray tubes placed with an interval of 100 mm between any two neighboring tubes. Fig. 3 shows the X-ray images of debris cloud at four typical moments when the 6061-T1 bumper is being normally impacted by a spherical AL-2017 projectile (Ø 3.2 mm) at 4.13 km/s.

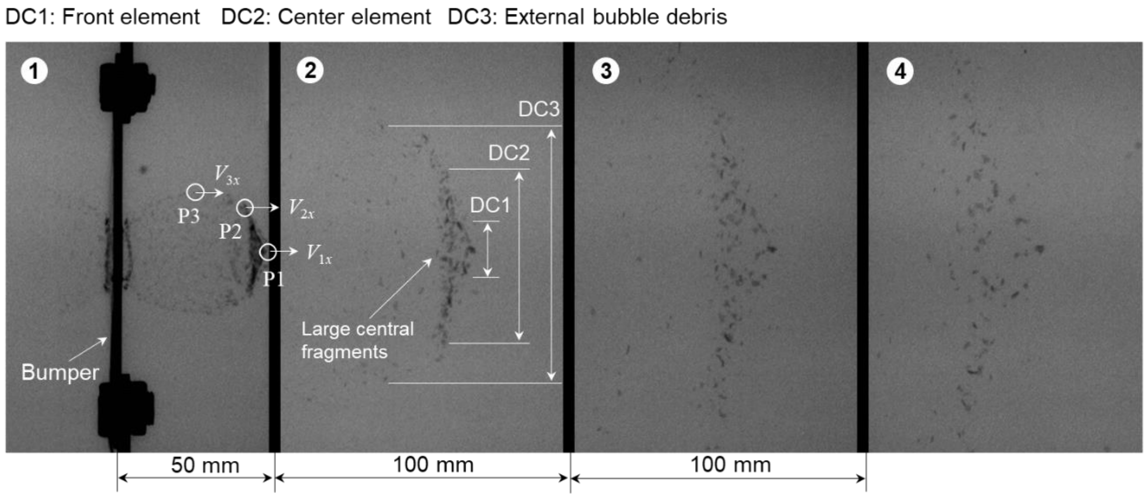

Fig. 3. X-ray images showing the formation and expansion of debris cloud under normal HVI.

Under normal HVI, the debris cloud is distributed symmetrically with a slow radial expansion, as observed in Fig. 3 and illustrated schematically in Fig. 4(a). The cloud comprises three major parts, namely an *ejecta veil*, an *external bubble debris*, and *a significant internal* *structure* (including a *front*, *center* and *rear element*). As observed, numerous particles are concentrated in the internal structure at the front of the bubble debris, with majority of large central fragments in the center element. The debris cloud further impinges the rear wall layer, and its front element, center element and external bubble debris jointly introduce multitudinous, disorderedly scattered pitting craters and cracks in the rear wall. The pitting damage area can be broadly classified into three areas: *the central cratered area* (D_{cc}), *the ring cratered area* (D_{rc}), and *the spray area* (D_{99}), respectively, as interpreted in Fig. 4(b). These three damage areas contain 99% of the pitting craters and cracks.

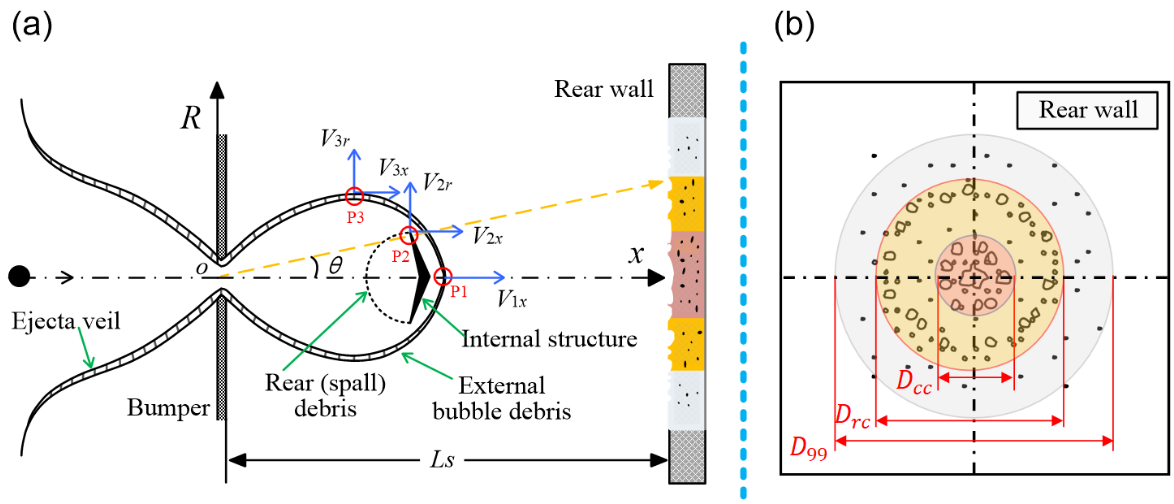

Fig. 4. Normal HVI case: (a) schematic of debris cloud structure; and (b) schematic of debris cloud-engendered pitting damage area in the rear wall layer (L_s : shield spacing).

The diameters of D_{cc}, D_{rc} and D_{99} are associated with the residual velocities of debris particles when they reach the rear wall. To investigate this, three feature points on the profile of debris cloud, viz., *the leading-edge point* (P1), *the maximum radial dimension point of internal structure* (P2), and *the maximum radial dimension point of external bubble debris* (P3), are defined to calculate both the radial and axial velocities using a sequence of radiographs of debris cloud. To benefit analysis, let V_{1x} signify the maximum velocity of the shattered particles in debris cloud at P1 along the axial direction, which is approximately

87%~91% of the incident velocity of the projectile when the shield spacing (L_s) is 100 mm and the thickness of bumper is 1 mm, according to authors' earlier studies [22-24]; let V_{3r} denote the maximum velocity in the radial direction, and V_{2x} the maximum velocity at P2 along the axial direction which is usually 85% of V_{1x}, and V_{3x} the maximum velocity at P3 along the axial direction which is 51%~60% of V_{1x}.

Besides the diameter above defined, the respective damage degrees of D_{cc}, D_{rc} and D_{99}, which depend on the distribution of debris cloud kinetic energy per area (*DCPKE*) $\overline{E}_s$, are relating to both the velocity and mass distribution, and can be obtained by [25]

$$\overline{E}_s = \frac{A_e e^{-2r^2/w_d^2 L_s^2}}{W_d L_s^2 \sqrt{\pi/2}}, \quad (1)$$

where r is the radial distance, L_s the shield spacing, A_e the maximum energy density, w_d the energy distribution parameter. According to the Eq. (1), the spatial distribution of $\overline{E}_s$ is analogous to that of debris cloud mass – being relatively higher near the cloud front along the *x*-axis, and decreasing sharply along the radial direction. Such distribution of *DCPKE* yields different degrees of strain rate and plastic deformation in the rear wall material over the pitting damage area (D_{cc}, D_{rc} and D_{99}), because the generation of strain rate is associated with the *DCPKE*: the higher the *DCPKE*, the greater intensification of the strain rate will be.

3.2. Morphological Characterization of Pitting Damage in Rear Wall

Representatively, Fig. 5 shows the debris cloud-induced pitting damage in rear wall layer. The sizes, severity degrees and patterns (multitudinous clustered, localized craters and cracks) of D_{cc}, D_{rc} and D_{99} clearly underline the effect of structural characteristics of debris cloud on generated damage. The diameters of these pitting damage areas are measured from the images of the rear wall. It is apparent in Fig. 5 that the morphology of debris cloud-induced pitting craters in D_{cc}, D_{rc} and D_{99} are irregular when compared against the hemispherical morphology of craters induced by a single projectile normal impact. To investigate this, three-dimensional (3D) morphological characterization of the pitting damage is conducted with the LSM featuring a spatial resolution of 10 μm. The diameters and depths of the craters are measured from the cross-sectional profiles of these 3D models (Fig. 6), to quantify the severity of these pitting craters. Two key observations from the 3D characterization are:

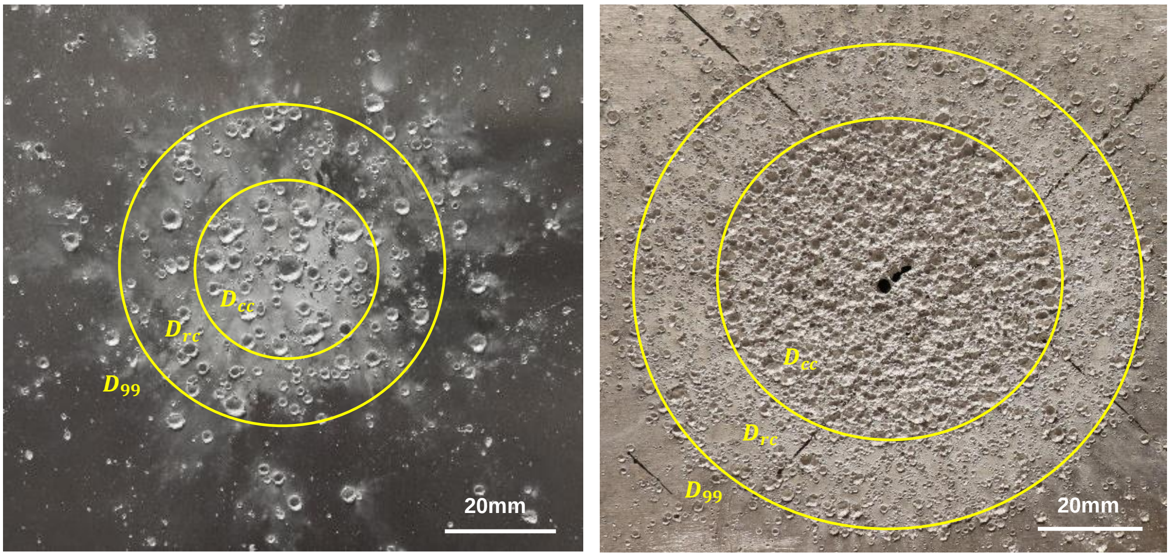

Fig. 5. Morphology of debris cloud-induced pitting damage in rear wall: (a) projectile speed: 4.13 km/s, diameter:3.2 mm (left); and (b) projectile speed: 5.93 km/s, diameter:4.5 mm (right).

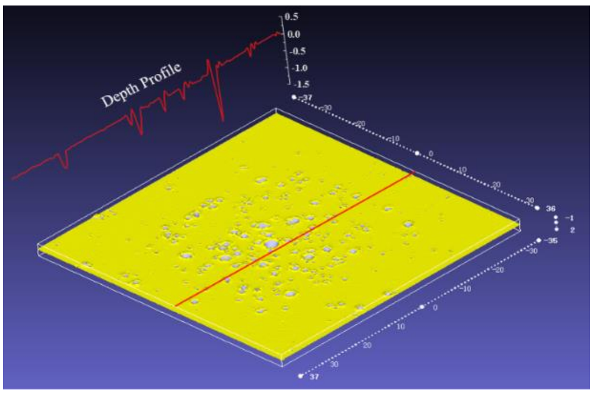

Fig. 6. 3D morphology of the pitting damage (projectile speed: 4.13 km/s, diameter:3.2 mm).

(1) when the initial velocity of the projectile is 4.13 km/s, primary craters (with a diameter close to the thickness of the rear wall) are mainly concentrated in D_{cc} (because majority of the large debris particles align in the center of debris cloud, as shown in Fig. 3); most sub-crates (with diameters between 1 mm and the thickness of rear wall) are in D_{rc}; and micro-craters (with diameters between tens to hundreds of microns) broadly scattered in all D_{cc}, D_{rc} and D_{99}, as revealed by Fig. 5(left). Fig. 7 shows the profiles of three representative pitting craters in D_{cc}, D_{rc} and D_{99}, respectively measuring ~2.3 mm, ~1.1 mm, and ~0.5 mm. The diameters of most pitting craters are larger than those of the debris particles (10~100 μm), which can be attributed to the fact that the material in the impact spot of rear wall further melts under high shock wave stress and dramatic elevation of temperature. In D_{cc}, visible macro-scale cracks are observed around the craters, along with deformation at the backside of the rear wall, implying a severe plastic deformation of the material in D_{cc} during HVI from the debris cloud;

(2) when the initial speed of the projectile increases to 5.93 km/s, massive tiny particles ranging from tens to hundreds of microns (even millimeters) are generated, resulting in a reduced number of primary craters whereas more sub-craters and micro-craters. At such a high impact velocity, the materials of projectile and bumper change to molten liquid droplets or vapor, and the damage degree, in terms of crater depths, is consequently mitigated, Fig. 5(right). To take a step further, the surface morphology of D_{cc}, D_{rc} and D_{99} is compared in Fig. 8, to observe that the surface of D_{cc} features a large number of pitting craters that are mutually nested and overlap another, Fig. 8(a) – caused by multiple collisions of debris particles and high temperature droplets. In D_{rc}, isolated sub-craters and numerous micro-craters are clearly observed, in Fig. 8(b), which are introduced to the rear wall by tiny debris particles, forming a rough and uneven pitting crater surface.

In D_{99}, small and shallow pitting craters with rough surfaces are noted, Fig. 8(c).

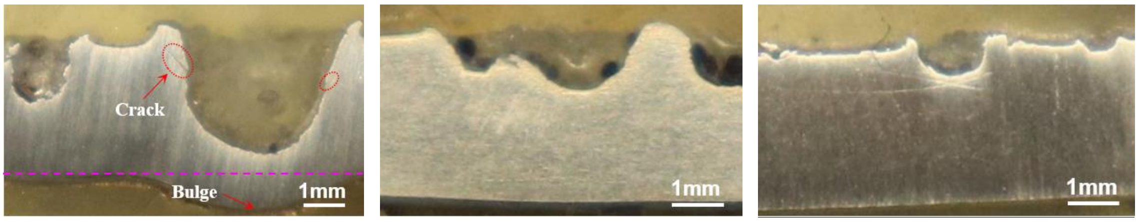

(a) (b) (c)

Fig. 7. Profile images of representative pitting craters in (a) D_{cc}; (b) D_{rc}; and (c) D_{99} (projectile speed: 4.13 km/s).

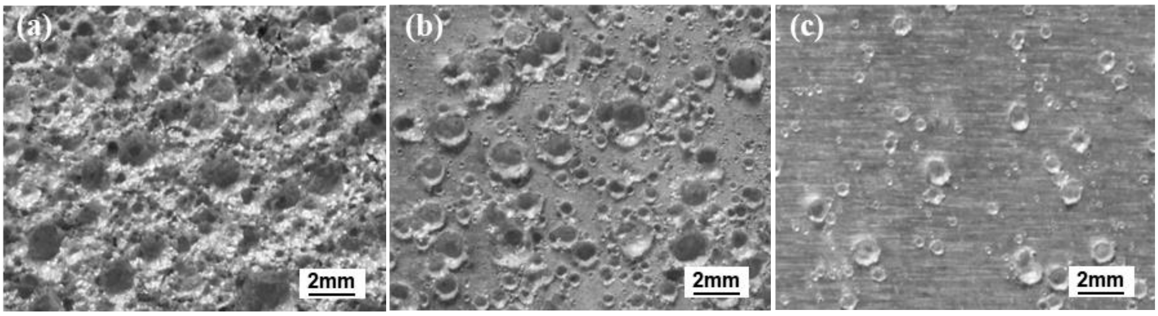

Fig. 8. Surface morphologies of (a) D_{cc}; (b) D_{rc}; and (c) D_{99} (projectile speed: 5.93 km/s).

3.3. Microstructural Characterization of Pitting Damage in Rear Wall

Microstructural characteristics of the debris cloud-committed pitting damage in rear wall are also investigated. D_{cc}, D_{rc} and D_{99} are respectively sectioned, mounted in epoxy, ground, polished, cleaned, and finally chemically etched with Keller solution of 25% HNO_3+15% HCl+10% HF +50% H_2O for ~30 seconds. Vickers micro-hardness beneath the pitting damage area is calibrated with an HVS-100 micro-hardness tester. Microstructural changes in the pitting craters are examined with OM (LEICA DFC-320) and SEM (JEOL JSM-6490) equipped with X-ray energy dispersive spectroscopy (EDS). XRD (Rigaku SmartLab®) analysis is conducted, and EDS is subsequently carried out to determine the type of elements.

3.3.1. Material Degradation

In the pitting damage area, in addition to those visible macroscopic craters and cracks, microstructural defect also manifests itself in diverse modalities, as observed in optical micrograph images. For illustration, Fig. 9 displays the microstructures beneath D_{cc}, D_{rc} and D_{99}, revealing numerous micro-voids and micro-cracks in the vicinity of pitting craters. It is the high pressure of HVI-induced shock waves (tens of GPa) – two orders of the magnitude higher than that of the strength of 5A06 alloy (~0.314 GPa) – that leads to the formation of cracks beneath the pitting crater, and this observation indicates that the material adjacent to the crater bottom undergoes severe plastic deformation during the debris cloud impact (Fig. 9(a)). The numerous micro-voids are a potential precursor to initiate macroscopic cracks (Fig. 9(b)), leading to material failure; and the micro-cracks nucleate and expand in a direction approximately 45° to the impact direction (Figs. 9(a) and (b)).

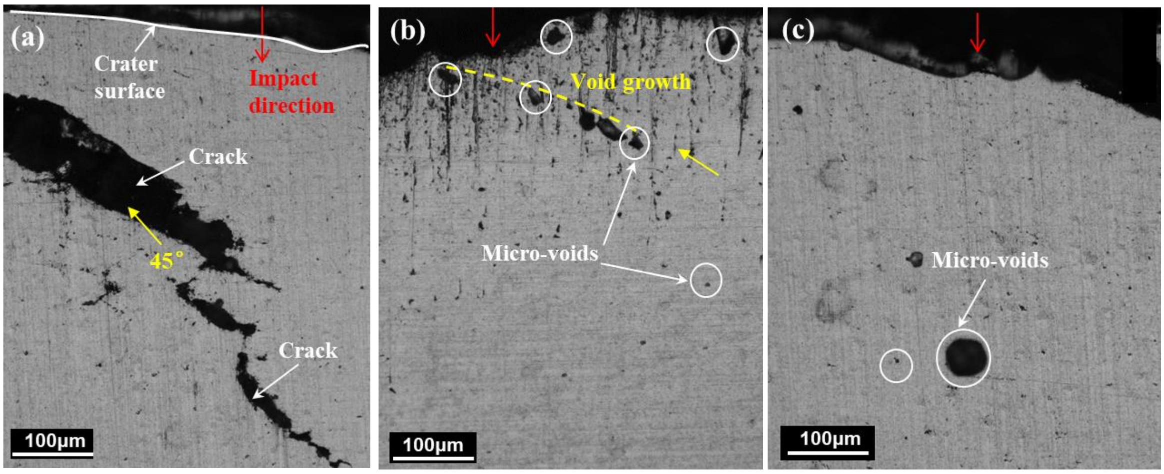

Fig. 9. Microstructural images beneath (a) D_{cc}; (b) D_{rc}; and (c) D_{99} (projectile speed: 4.13 km/s).

The micrographs showing the microstructure of the material in D_{cc} are presented in Figs. 10(a) and (b), in which compressive-type damage regions of concavity shapes are observed adjacent to the craters bottom, along with numerous micro-voids distributed along the flown lines. The concavity shape of these flown lines argues that the wavefront of HVI-induced shock waves normal to the target panel are spherical or quasi-spherical. High pressure and high temperature near the impact site make the material behave like an ideal uncompressible fluid or viscous fluid, while such a fluid-like property of the material is weakened dramatically away from the crater bottom, because the plastic strain attenuates remarkably, leading to the change in the shape of the flown lines from concavity to near flat planes (see Fig. 10(c)). Simultaneously, a series of parallel fluid layers with different flowing velocities are created, resulting in the generation of whirlpool-like bands beneath the pitting craters, as observed in Fig. 10(d).

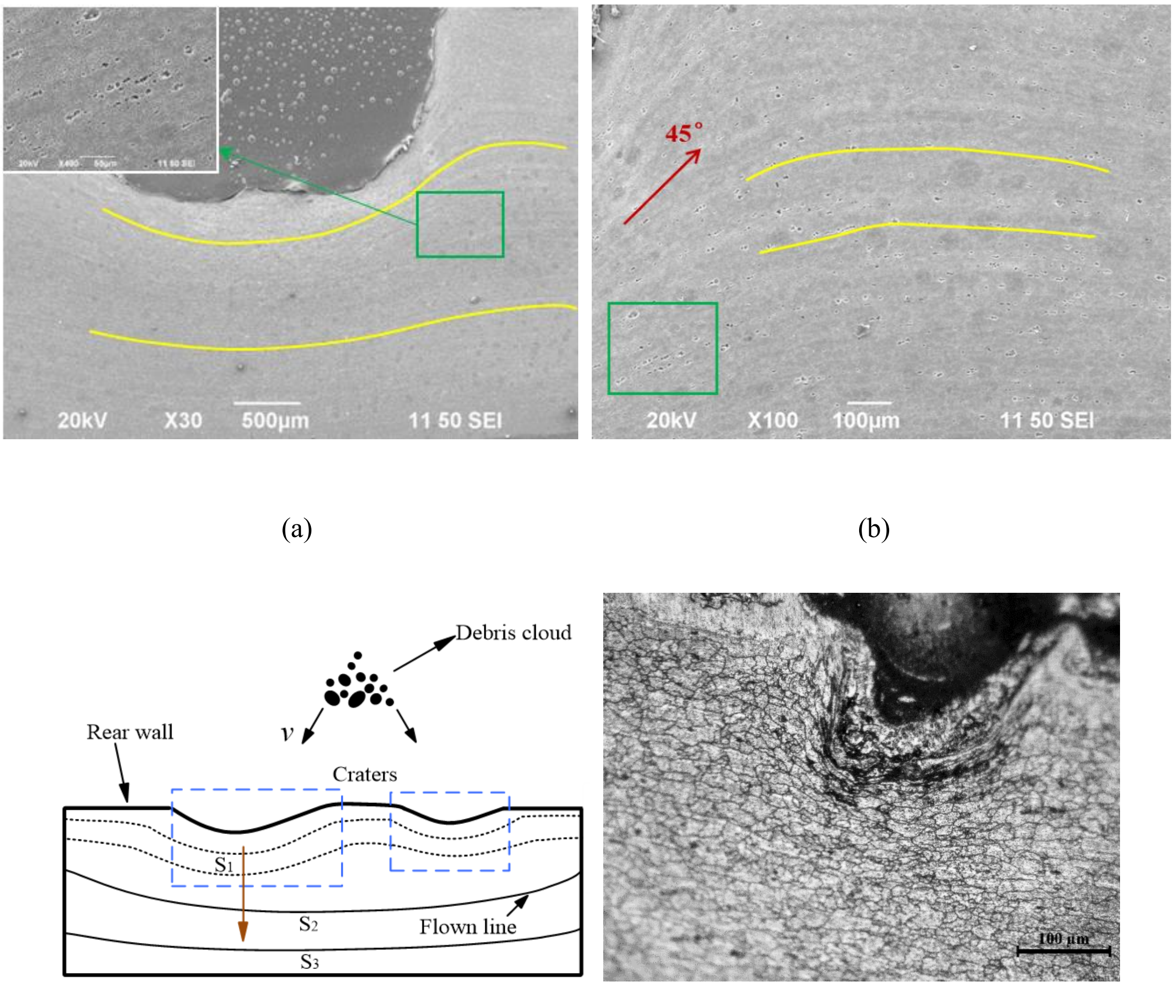

(a) (b)

(c) (d)

Fig. 10. (a) Microstructure of material under craters in D_{cc}; (b) microstructure of material between two craters in D_{cc}; (c) schematic description of debris cloud-induced shock wave propagation; and (d) optical image of the whirlpool-like bands (projectile speed: 4.13 km/s).

The SEM image of material in D_{cc} is shown in Fig. 11, unveiling that distinct fine grains are generated in the microstructure of material beneath the crater bottom, and the average grain sizes are ~2 μm in region I (nearest to the pitting crater bottom), ~10 μm in region II, and ~20 μm in region III (furthest to the pitting crater bottom), as marked in Fig. 11(a), compared with the average size of the original grains of ~40 μm (Fig. 2) prior to HVI. The smaller the grain size the more severe the degree of compression to the material will be; the further the distance from the pitting crater bottom, the less compressive plastic deformation of the material it is, as seen in Fig. 11(a). This observation suggests that non-uniform plastic deformation and localized recrystallization occur along the impact direction (see red arrow in Fig. 11(a)) when the debris cloud impacts the rear wall. The SEM image of the marked region I is displayed in Fig.11(b), showing that the original grains in D_{cc} are markedly fragmentated, and then recrystallized, leading to the nucleation of fine grains and serrated heaves under the effect of high storage energy induced by the plastic deformation.

Also observed in Fig. 11(a) are multitudinous micro-voids at the grain boundaries and within the grains. The number and size of micro-voids in the coarse grain regions II and III are observed larger than those in the fine grain region I, because material in region I undergoes the strongest effect from the shock wave, resulting in micro-voids shrinking and even disappearance; the shock waves are reflected from the back surface of the rear wall to form a rarefaction wave (tensile-type), giving rise to expansion of micro-voids in region III and II. The sizes of micro-voids at the grain boundaries are generally smaller than those within the grains, due to the effect of concentrated stress and higher distortion energy at the grain boundaries.

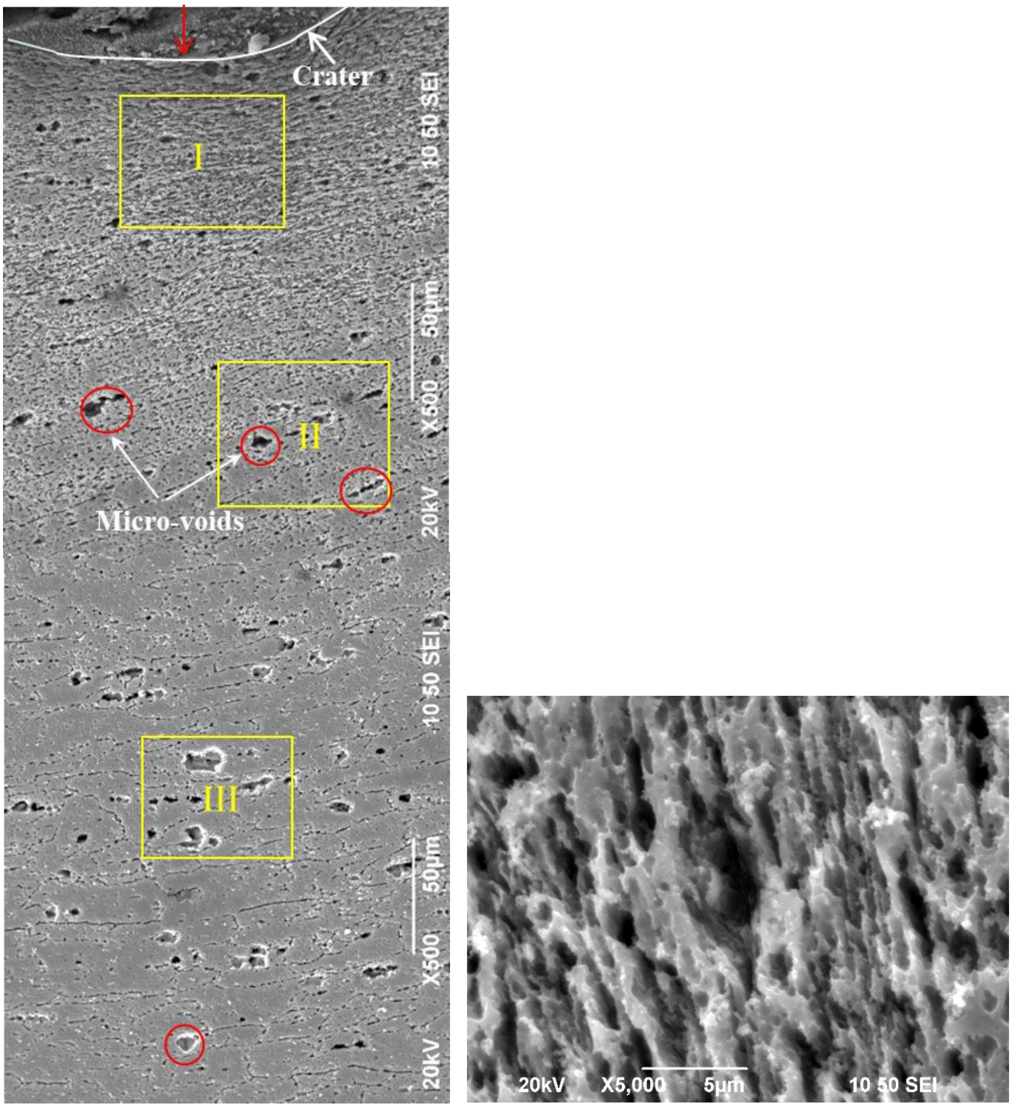

(a) (b)

Fig. 11. (a) SEM image of material beneath the crater bottom in D_{cc}; and (b) zoomed-in part of region I in (a) (projectile speed: 4.13 km/s).

Figures 12 and 13 display the SEM images of materials in D_{rc} and D_{99}, respectively. Compared with the microstructure of material in D_{cc} (Fig. 11(a)), that in D_{rc} (Fig. 12) is moderately deformed, and the one in D_{99} (Fig. 13) is slightly deformed. That is because the *DCPKE* follows a gaussian distribution (as interpreted in Section 3.1), squeezing gradually along the radial direction away from the pitting damage center. As observed in SEM, the micro-voids are visible in all D_{cc}, D_{rc} and D_{99}, while fine grains can only be captured in the severely compressed region I adjacent to the crater bottom, in particular in D_{cc} (~ 2 μm), as marked in Figs. 11(a), 12 and 13. The average sizes of grains are ~ 5 μm in region I of D_{rc}, ~ 10 μm in region I of D_{99}, respectively, indicating that the grain size increases progressively as shock stress decreasing in different pitting damage area.

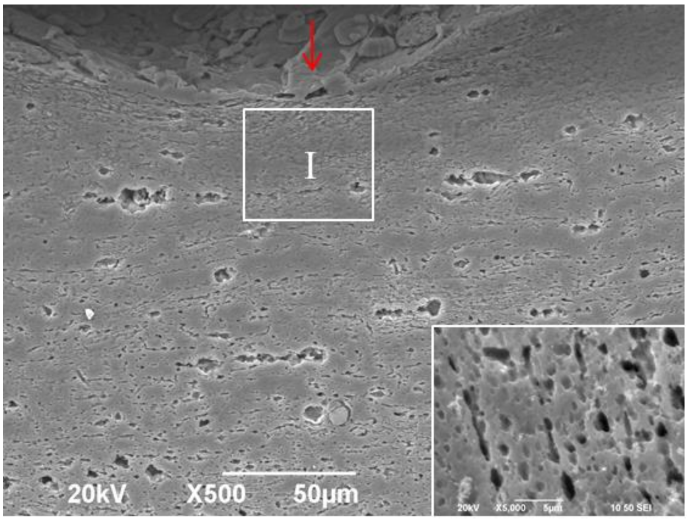

Fig. 12. SEM image of material beneath the crater in pitting damage area in D_{rc} (projectile speed: 4.13 km/s).

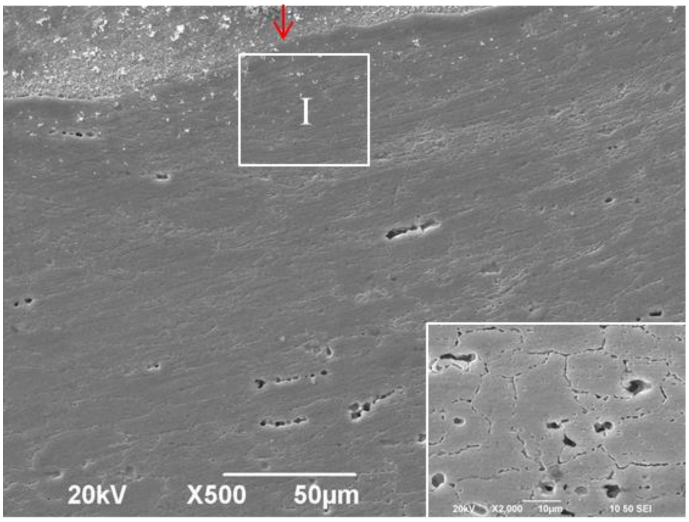

Fig. 13. SEM image of material beneath the crater in pitting damage area in D_{99} (projectile speed: 4.13 km/s).

It is also relevant to note that both the number of micro-voids and their volume fraction, in coarse grain regions (*i.e.*, regions II and III, 200 μm away from the crater bottom) in D_{cc}, D_{rc} and D_{99}, are all increased dramatically as the plastic deformation intensifies, indicating the accumulation of micro-damage during debris cloud-induced HVI, as seen in Fig. 14.

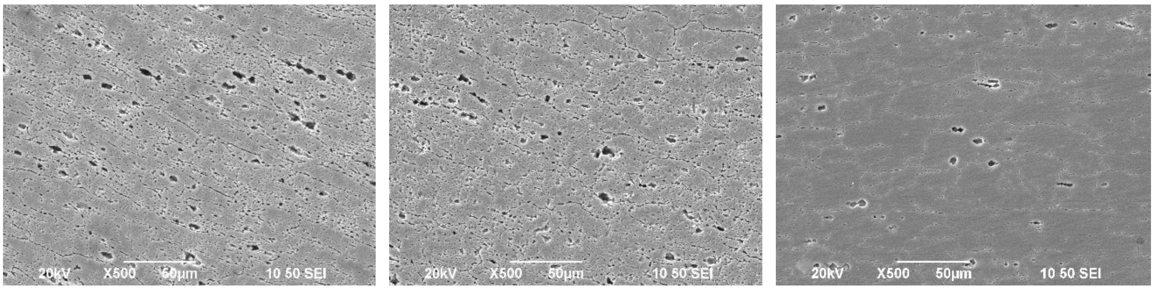

(a) (b) (c)

Fig. 14. SEM images of materials in different pitting damage areas, 200μm away from the crater bottom: (a) D_{cc}; (b) D_{rc}; and (c) D_{99} (projectile speed: 4.13 km/s).

3.3.2. Micro-void Progress

When debris cloud impacts the rear wall, the shock waves generate high strain rate (~ $10^6 \sim 10^8$ s^{-1}), high shock stress (~10~200 GPa), high temperature (~400~5000 K) and large deformation (~10~35% compression ratio), which deteriorate the intrinsic defects in the material (in the modality of micro-voids), more remarkably at the second-phase particles, inclusions and grain boundaries [5]. Fig. 15(a) presents the SEM image of the material in D_{cc}, showing the void nucleation and propagation in this region under HVI, which consists of three key stages:

(1) void nucleation: voids are initiated at the grain boundaries and within grains, or deteriorate from existing material defects during large plastic deformation;

(2) void expansion: the severely compressed material exhibits strong tendency to remain its original state, and this leads to the generation of instantaneous unloading shock waves

(tensile-type), accompanying with residual stresses and reflected rarefaction waves (tensile-type). Together, all these factors drive voids to expand;

(3) void coalescence and material fracture: voids expand under a tensile-type wave converted from HVI-induced shock wave, and adjacent voids coalesce and join together to form inter-granular and trans-granular micro-cracks, as interpreted in Fig. 15(b). The void coalescence can eventually result in the presence of macroscopic cracks and failure of the material.

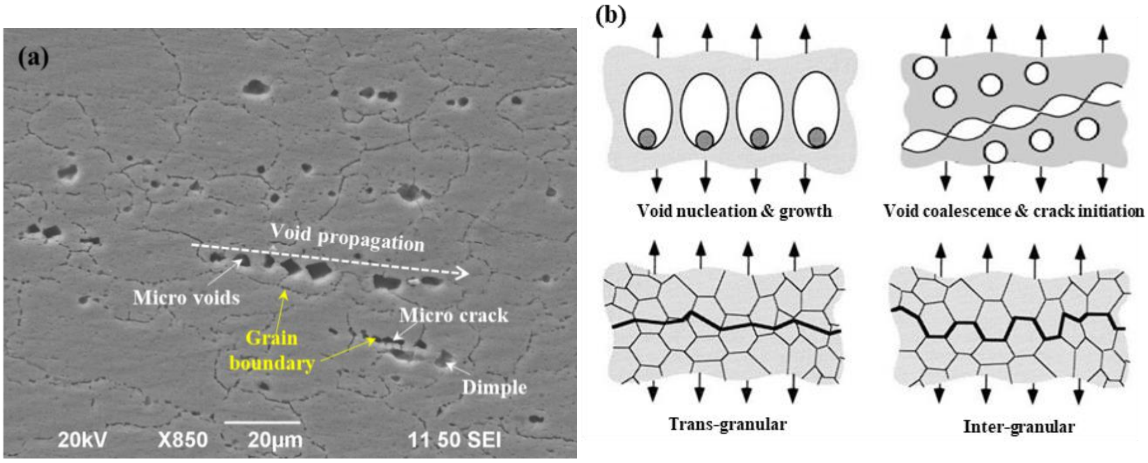

Fig. 15. (a) SEM image of material in D_{cc}, showing void nucleation and propagation; and (b) schematic of void nucleation, growth and coalescence [26-28].

As observed in Fig. 15(a), all micro-voids feature near spherical shapes with smooth surfaces, and that is because under the elevated temperature during HVI, the material within the micro-voids melts. It is surmised that under an extremely high shock stress, more dislocation cells exist in the material, introducing stress concentration at grain boundaries and further grain boundary slip. As a result, the initiation of micro-voids and formation of recrystallization nucleus take place at grain boundaries first. The coalescence of grain boundaries further gives rise to the micro-void shrinking or disappearance. Consequently, fewer micro-voids with smaller sizes (micron in diameter) can be observed at grain boundaries, in Fig. 15(a).

The evolution of micro-voids in the pitting damage area progressively deteriorates the material of the rear wall layer, and the macroscopic mechanical property of material is therefore degraded upon HVI. The material degradation progress, reflected by the ratio of the void volume fraction to time, is governed primarily by the nucleation rate of the newly generated voids by HVI ($\dot{f}_{HVI}$) and the expansion rate of the pre-existing voids (material defects) ($\dot{f}_{defect}$) that can be defined using the Gurson-Tvergaard-Needleman (GTN) model as detailed elsewhere [29-32]

$$\dot{f} = \dot{f}_{HVI} + \dot{f}_{defect}, \tag{2}$$

In particular, $\dot{f}_{HVI}$ can be calibrated by

$$\dot{f}_{HVI} = \frac{f_N}{s_N\sqrt{2\pi}}\exp\left[-\frac{1}{2}\left(\frac{\varepsilon^p - \varepsilon_N}{s_N}\right)\right]\dot{\varepsilon}^p, \tag{3}$$

where f_N denotes the limit of volume fraction of the potential nucleating voids, ε_N the mean equivalent plastic strain for nucleation, s_N the corresponding standard deviation, ε^p the von Mises plastic strain, and $\dot{\varepsilon}^p$ the von Mises plastic strain rate. On the other hand, $\dot{f}_{defect}$ is defined by

$$\dot{f}_{defect} = (1 - f_v)\dot{\varepsilon}^p_{kk}, \tag{4}$$

where $\dot{\varepsilon}^p_{kk}$ is the hydrostatic component of macroscopic plastic strain rate, and f_v the current void volume fraction. From Eq. (4), it is apparent that the nucleation and expansion of micro-voids are associated with the plastic strain rate $\dot{\varepsilon}^p_{kk}$. The above analysis implies that the material manifests different degrees of plastic strain rate in D_{cc}, D_{rc} and D_{99}, leading to the discrepancy in void volume fractions in these three areas. The higher the strain rate, the more micro-voids will be formed. This observation is in good agreement with that from the metallographic analysis (Fig. 14).

3.3.3. Micro-void Identification **(EDS Analysis)**

Spot analysis and line scanning tests are conducted using EDS on the material extracted from the rear wall, to identify and determine quantitatively the chemical compositions of the material in the pitting damage area. The EDS line scanning result, Fig. 16(a), shows that the concentration of the element AL decreases significantly at voids (①, ③ and ④) and also at the crack along grain boundary (②), which once again corroborates earlier statement that the debris cloud-induced the pitting damage features voids and cracks. EDS spectrum analysis result, Fig. 16(b), illuminates the proportion of material compounds at three different testing points where a void exists or not. The results highlight that the compound compositions of materials at all testing points are similar, and only the proportion of element is slightly different.

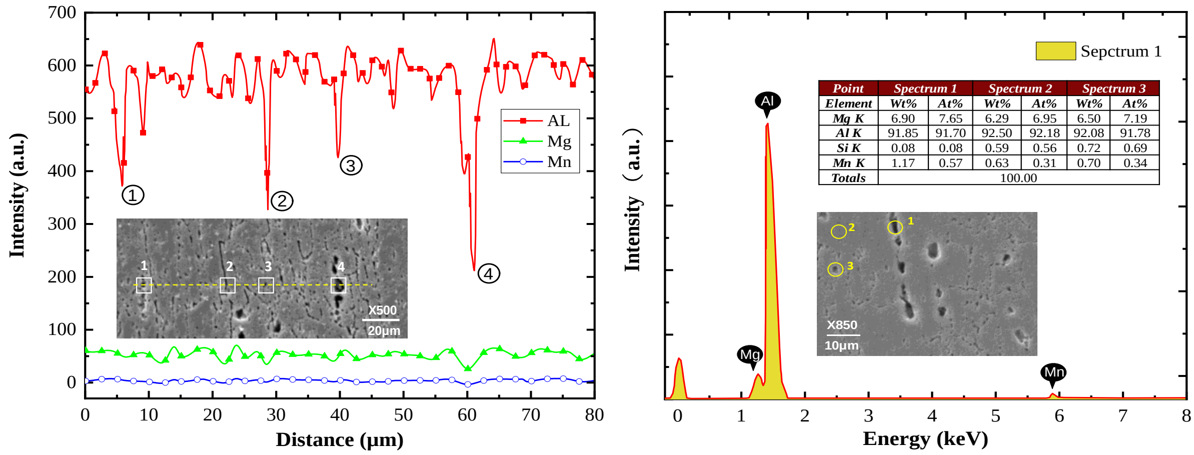

Point	Spectrum 1		Spectrum 2		Spectrum 3	
Element	Wt%	At%	Wt%	At%	Wt%	At%
Mg K	6.90	7.65	6.29	6.95	6.50	7.19
Al K	91.85	91.70	92.50	92.18	92.08	91.78
Si K	0.08	0.08	0.59	0.56	0.72	0.69
Mn K	1.17	0.57	0.63	0.31	0.70	0.34
Totals	100.00					

(a) (b)

Fig. 16. (a) EDS line scanning analysis result; and (b) EDS spectrum (wt%: weight percentage, At.%: atomic percentage) (projectile speed: 4.13 km/s).

3.3.4. Micro-hardness Distribution of Pitting Damage Areas

Micro-hardness of the rear wall layer containing pitting damage is calibrated at a series of testing points along the wall thickness with the first point being 0.1 mm below the pitting crater bottom. Fig. 17 shows the obtained micro-hardness distribution, to observe that the extents of micro-hardness of D_{cc} , D_{rc} and D_{99} are higher than that of the base metal

(HV85) of the rear wall, which can be attributed to the intensification of the strain and strain-rate hardening effects due to HVI. The micro-hardness drops away from the pitting crater bottom. The SEM images, Fig. 11, show that the grain structures beneath the craters are flattened, namely *shock hardened* – meaning higher micro-hardness. That is because during HVI the local melting and rapid cooling of the material can refine the grains adjacent to the pitting crater bottom, accompanying with plastic deformation and augment in material density. By way of illustration, the micro-hardness of the material near the pitting crater in D_{cc} is 136.8 HV – that is 1.6 times the hardness of the base metal.

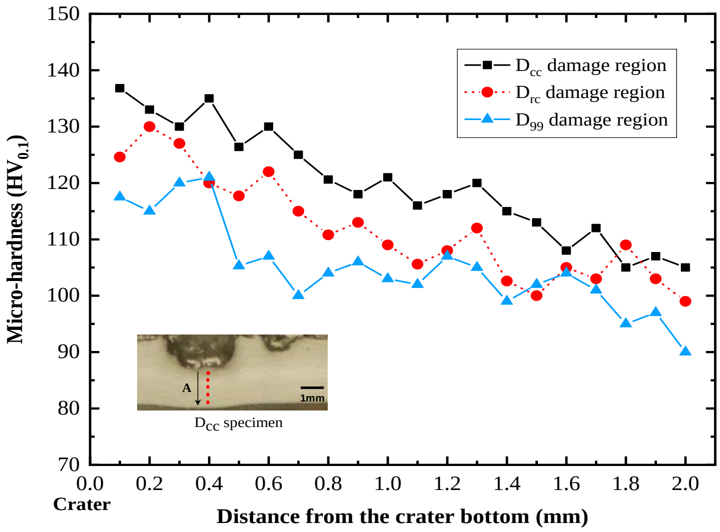

Fig. 17. Micro-hardness distribution of materials in D_{cc}, D_{rc} and D_{99} (projectile speed: 4.13 km/s).

3.3.5. Dislocation Density

To investigate the changes in the dislocation density of material in D_{cc}, D_{rc} and D_{99}, XRD analysis is implemented, and representative (311) diffraction peaks are shown in Fig. 18. Compared with that of the base metal of the rear wall, the intensities of diffraction peaks for the material in D_{cc}, D_{rc} and D_{99} are observed largely unchanged, while the peak angle shifts upward and the peak width increases significantly. This upward shift of the peak angle represents a decrease in the (311) plane spacing in the compression direction of the plate; while the increase in the diffraction peak width implies that the dislocation density augments, as a result of plastic deformation in the material.

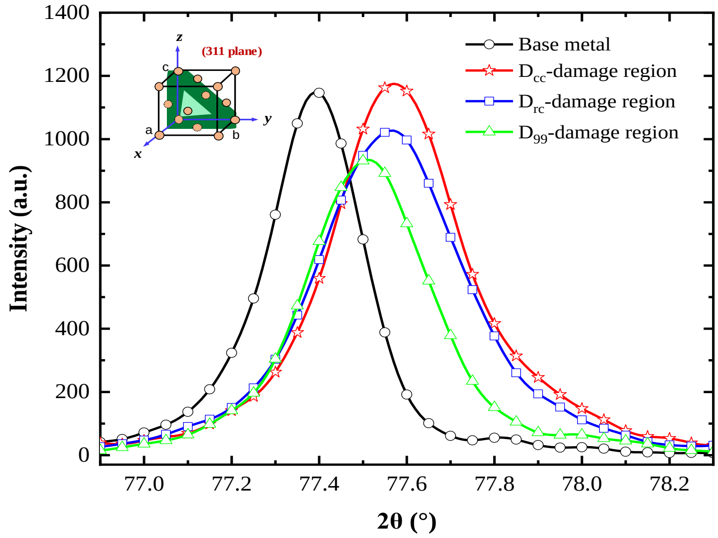

Fig. 18. Representative (311) diffraction peaks for materials in base metal, D_{cc}, D_{rc} and D_{99} (projectile speed: 4.13 km/s).

The dislocation density ρ_{dis} can be defined as [33]

$$\rho_{dis} = \frac{\chi^2}{2\pi b^2 \cdot \text{In}2}, \tag{5}$$

where b denotes the Burgers vector ($b = 0.286$ nm for the aluminium used in this study), and χ the full width at half maximum (FWHM) of diffraction peak. With Eq. (5), ρ_{dis} is calculated to be 0.566×10^{14} m^{-2} for the base metal, and 1.183×10^{14} m^{-2}, 1.053×10^{14} m^{-2} and 0.881×10^{14} m^{-2} for the materials in D_{cc}, D_{rc} and D_{99}, respectively. It is apparent that the dislocation densities of material in pitting damage areas are higher than that of the base metal.

In addition, the relation between FWHM χ and heterogeneous strains ε can be ascertained by the Williamson-Hall equation [34] as

$$\chi \cdot \frac{\cos\theta}{\lambda_w} = \frac{0.9}{d} + \varepsilon \cdot \frac{\sin\theta}{\lambda_w}, \tag{6}$$

where θ is the diffraction angle, λ_w the wavelength of the incident X-ray ($\lambda_w = 0.15405\ \text{nm}$), and d the average crystallite size. Using Eq. (6), the Williamson-Hall plot of materials in D_{cc}, D_{rc} and D_{99} are obtained and displayed in Fig. 19, revealing that materials in different regions have different strains – reflected by distinct slopes of the curves. With the increase of *DCPKE* in D_{cc}, D_{rc} and D_{99}, the degree of pitting damage is intensified, resulting greater heterogeneous strains.

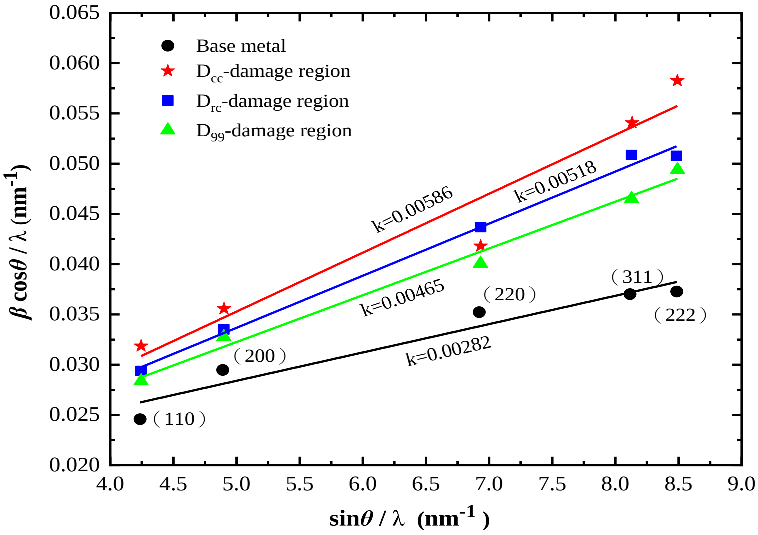

Fig. 19. Williamson-Hall plot of materials in base metal, D_{cc}, D_{rc} and D_{99} (projectile speed: 4.13 km/s).

4. Discussions

4.1. Shock Wave Effect

During the debris cloud impinges the rear wall, shock wave will be generated in all the debris particles and the rear wall plate as well. Let *S1* denote the shock wave propagating in a debris particle and *S2* the wave in the plate, as illustrated schematically in Fig. 20(a). The high pressure associated with shock wave propagation is typically several orders of the material strength of the plate. As a result, both the debris particle and plate will be severely compressed and materials intend to remain their original status, consequently generating tensile-type unloading wave (*R1*). If the tensile stress of *R1* is higher than that of the particle or plate, the material of the particle or plate will be shattered and spatter out, leading to the formation of a thin outer fringe around the mouth of the crater. Simultaneously, tensile-type damage such as dimples, micro-voids and micro-cracks, will be engendered in the rear wall adjacent to the craters, as seen in Figs. 9 and 11. However, the shock wave *S2* will be reflected from the back surface of the plate to create a tensile-type shock wave *R2,* as shown in Fig. 20(b). Due to the tensile effect of *R2*, the material near the back surface of the plate will “swell”. Spall and protuberance will be induced if the stress of *R2* is lower than the tensile strength of the material of the plate whereas higher than the limit of spall [35].

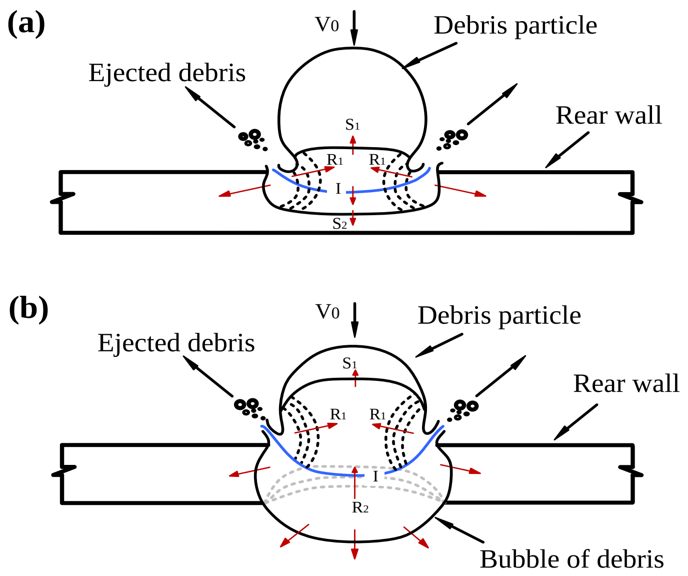

Fig. 20. (a) Debris cloud-induced shock waves in a debris particle and the rear wall; and (b) shock wave reflected from the back face of rear wall.

According to the authors’ earlier studies [23], the shock compression stress (p_{HVI}) under debris cloud HVI can be defined by

$$p_{HVI} = \rho_0 \frac{V_0}{2}(c_0 + 1.338\frac{V_0}{2}), \quad (7)$$

where ρ_0 denotes the material density ($\rho_0 = 2640\ \mathrm{kg/m^3}$ for 5A06 alloy), c_0 the speed of sound in the selected material ($c_0 = 5328$ m/s), and v_0 the velocity of debris particle at which the particle impacts the target plate. v_0 of a particle impacting D_{cc}, D_{rc} or D_{99} can be deemed as the particle velocity at P1, P2 or P3 in Fig. 3. By way of illustration, at a given initial impact speed of 4.13 km/s for a projectile with a dimeter of 3.2 mm, v_0 is 3.56 km/s, 3.03 km/s or 2.14 km/s, respectively in D_{cc}, D_{rc} or D_{99}. According to Eq. (7), p_{HVI} is 36.23 GPa, 29.42 GPa and 19.09 GPa, respectively for D_{cc}, D_{rc} and D_{99}. Taking a step further, the compression ratio (η) of the material can be obtained by [36]

$$p_{HVI} = \rho_0 c_0^2 \frac{\eta}{(1-1.338\eta)^2}, \tag{8}$$

Using the above example, the compression ratios of the materials are 0.231, 0.206 and 0.158, respectively in D_{cc}, D_{rc} and D_{99}.

4.2. Dynamic Recrystallization

Upon HVI, the rear wall is severely compressed by the shock wave *S2*, resulting in plastic deformation. The deformed material is thermo-dynamically instable, and it contains high distortion energy for recrystallization. The other condition for recrystallization is temperature, which can be achieved via two means: either the adiabatic compression during shock wave propagation (*i.e.* shock heating) or the plastic deformation (*i.e.* plastic work heating). Temperature that results in recrystallization process in metals can be calculated by [37]

$$T = 0.4 \sim 0.5\, T_m, \tag{9}$$

where T_m is the melting point of the material. For 5A06 alloy ($T_m = 960\,\mathrm{K}$), one has $T = 384 \sim 480\,\mathrm{K}$.

Shock temperature (T_{HVI}) can be calculated by [36]

$$T_{HVI} = T_0 \exp(2\eta) + \frac{c_0^2}{c_v} \exp(2\eta) \int_0^{\eta} \frac{1.338x^2}{(1-1.338x)^3} \exp(-2x)\, dx, \tag{10}$$

where T_0 signifies the room temperature and c_v the specific heat capacity ($c_v = 921\ \mathrm{J/kg\cdot °C}$). For illustration, at a given initial impact speed of 4.13 km/s for a projectile with a dimeter of 3.2 mm, the shock temperatures at different pitting damage areas, calculated using Eq. (10), are 873.5 K, 830.5 K and 754.5 K, respectively in D_{cc}, D_{rc} and D_{99}. These temperatures are nearly two times the recrystallization temperature of the material, speculating that temperature elevation induced by the shock heating has a non-negligible effect on the recrystallization of material beneath the craters.

When the strain-rate is larger than $10^3\ \mathrm{s^{-1}}$, all the plastic deformation energy can be transformed into heat, leading to the adiabatic temperature rise. Therefore, the rising rate of adiabatic temperature caused by the plastic deformation is represented as [9],

$$\frac{dT}{dt} = \frac{S_{ij}}{c_v\,\rho_0} \cdot \frac{d\gamma}{dt}, \tag{11}$$

where S_{ij} denotes the stress component (assumed to be equal to the tensile strength $\sigma = 420\ \mathrm{MPa}$), $d\gamma / dt$ the deformation strain-rate of the target material ($10^6 \sim 10^8\ \mathrm{s^{-1}}$), acquiring $dT / dt = 1.7 \times (10^8 \sim 10^{10})\ \mathrm{°C/s}$. Temperature raising rate of material induced by plastic deformation under debris cloud HVI is very high, indicating that the temperature for recrystallization is mainly caused by the plastic deformation storage energy. Shock wave loading and release occur within micro-seconds or even nanoseconds, and the 5A06 alloy has good thermal conductivity ($k = 167\ \mathrm{W/(m\cdot K)}$), leading to rapid cooling of the material away from the crater bottom. Therefore, the recrystallization that occurs during HVI is localized and dynamic.

5. Conclusions

The microstructural characterization of debris cloud-induced pitting damage in the rear wall of a typical dual-layered Whipple shield is studied via HVI experiment and a series of metallographic analysis including OM, LSM, SEM and XRD. The following conclusions and observations can be drawn:

(1) debris cloud-induced pitting damage features hundreds of clustered and localized craters disorderedly scattered over a wide area in the rear wall layer. The modality, pattern and severity of which are related to the impact velocity and projectile size. This pitting damage gives rise to material degradation which manifests different degrees in the central cratered area (D_{cc}), the ring cratered area (D_{rc}), and the spray area (D_{99}), respectively;

(2) fine grains beneath the pitting craters can be observed, which are prone to HVI-induced dynamic recrystallization. Dislocation cells formed during the HVI process act as the nuclei of dynamic recrystallization. The degree of recrystallization and dislocation decrease from the crater bottom and pitting damage center, dependent on strain rate levels;

(3) two modalities of damage, from micro-voids to micro-cracks, are generated in the pitting damage region. Whirlpool-like bands and micro-cracks exist around craters due to the high strain rate induced by shock waves. Micro-voids initiated at grain boundaries and within grains due to nucleation of grains and pre-existing material defects under extremely high compressive strain rate. Micro-voids coalesce and join together to form micro-cracks under tensile-type shock waves;

(4) micro-hardness of material in D_{cc} is higher than those in D_{rc} and D_{99}, and higher

micro-hardness is observed in the deformed region adjacent to the crater bottom compared against that in the region near the back surface of rear wall, due to strain hardening and refined grain under HVI.

Acknowledgments

This project was funded by the National Natural Science Foundation of China (Nos. 51635008, 11772113 and 51875492) and the Hong Kong Research Grants Council via General Research Fund (Nos. 15201416 and 15212417).

References

[1] Space.com.https://www.space.com/23039-space-junk-explained-orbital-debris-infographic.html.

[2] Christiansen EL, Hyde JL, Bernhard RP. Space shuttle debris and meteoroid impacts. Adv Space Res. 2004; 34(5): 1097-1103.

[3] IADC WG. Sensor Systems to Detect Impacts on Spacecraft. tech. rep., Report No. IADC-08-03, 2013.

[4] Zook HA. Deriving the velocity distribution of meteoroids from the measured meteoroid impact directionality on the various LDEF surface. Proceedings of the First Post-retrieval Symposium 1992; p569-579.

[5] Eftis J, Carrasco C, Osegueda RA. A constitutive-microdamage model to simulate hypervelocity projectile-target impact, material damage and fracture. Int J Plast 2003; 19(9): 1321-1354.

[6] Christiansen EL. Design and performance equations for advanced meteoroid and debris shields. Int J Impact Eng 1993; 14(1-4): 145-156.

[7] Iyer KA, Poormon KL, Deacon RM, Mehoke DS, Swaminathan PK, Brown RC. Hypervelocity impact response of Ti-6Al-4 V and commercially pure titanium. Procedia Eng 2013; 58: 127-137.

[8] Murr LE, Ayala A, Niou CS. Microbands and shear-related microstructural phenomena associated with impact craters in 6061-T6 aluminum. Mater Sci Eng. A-Struct Mater Prop Microstruct Process 1996; 216(1-2): 69-79.

[9] Zhen L, Li G, Zhou J, Yang D. Micro-damage behaviors of Al-6Mg alloy impacted by projectiles with velocities of 1~3.2 km/s. Mater Sci Eng. A-Struct Mater Prop Microstruct Process 2005; 391(1-2): 354-366.

[10] Liang X, Li H, Huang L, Hong T, Ma B, Liu Y. Microstructural evolution of 2519-T87

aluminum alloy obliquely impacted by projectile with velocity of 816 m/s. Trans Nonferrous Met Soc China 2012; 22(6): 1270-1279.

[11] Zou D, Zhen L, Zhu Y, Xu C, Shao W, Pang B. Deformed microstructure and mechanical properties of AM60B magnesium alloy under hypervelocity impact at a velocity of 4 km/s. Mater Sci Eng. A-Struct Mater Prop Microstruct Process 2010; 527(15): 3323-3328.

[12] Zou D, Zhen L, Zhu Y, Xu C, Shao W, Pang B. Deformed microstructure evolution in AM60B Mg alloy under hypervelocity impact at a velocity of 5 km/s. Mater Des 2010; 31(8): 3708-3715.

[13] Mendoza I, Villalobos D, Alexandrov BT. Crack propagation of Ti alloy via adiabatic shear bands. Mater Sci Eng. A-Struct Mater Prop Microstruct Process 2015; 645: 306-310.

[14] Hu J, Xuan F, Liu C. A void growth model of multiaxial power-law creep rupture involving the void shape changes. Int J Mech Sci 2018; 144: 723-730.

[15] Nikbin K, Liu S. Multiscale-constraint based model to predict uniaxial/multiaxial creep damage and crack growth in 316-H steels. Int J Mech Sci 2019; 156: 74-85.

[16] Cour-Palais BG. Hypervelocity impact in metals, glass and composites. Int J Impact Eng 1987; 5(1-4): 221-237.

[17] Schonberg WP. Protecting spacecraft against meteoroid/orbital debris impact damage: an overview. Space Debris 1999; 1(3): 195-210.

[18] Drolshagen G. Impact effects from small size meteoroids and space debris. Adv Space Res 2008; 41(7): 1123-1131.

[19] Horz F, Cintala MJ, Bernhard RP, Cardenas F, Davidson WE, Haynes GS, Thomas H, Winkler, JL. Penetration experiments in aluminum 1100 targets using soda-lime glass projectiles. NASA STI/Recon Technical Report N 1995; 96.

[20] Liu M, Wang K, Lissenden CJ, Wang Q, Zhang Q, Long R, Su Z, Cui F. Characterizing hypervelocity impact (HVI)-induced pitting damage using active guided ultrasonic waves:

from linear to nonlinear. Materials 2017; 10(5): 547.

[21] Destefanis R, Faraud M, Trucchi M. Columbus debris shielding experiments and ballistic limit curves. Int J Impact Eng 1999; 23(1): 181-192.

[22] Chi R, Pang B, Guan G, Yang Z, Zhu Y, He M. Analysis of debris clouds produced by impact of aluminum spheres with aluminum sheets. Int J Impact Eng 2008; 35(12): 1465-1472.

[23] Chi R. Research and modeling of debris cloud produced by hypervelocity impact of projectile with thin plate. Harbin, China, Harbin Institute of Technology, 2010.

[24] Guan G, Pang B, Zhang W, Ha Y. Crater distribution in the rear wall of AL-Whipple shield by hypervelocity impacts of AL-spheres. Int J Impact Eng 2008; 35(12): 1541-1546.

[25] Jia G, Hai H. Characters on kinetics energy of debris cloud in spacecraft. Journal of Beijing University of Aeronautics and Astronautics 2007; 33(3): 257.

[26] Levanger H. Simulating ductile fracture in steel using the finite element method: comparison of two models for describing local instability due to ductile fracture. Oslo, Norway, University of Oslo, 2012.

[27] Anderson TL, and Anderson TL. Fracture mechanics: fundamentals and applications (3rd Edition). Boca Raton: CRC press; 2005.

[28] Strąkowski M, Kamiński M. Stochastic Finite element method elasto-plastic analysis of the necking bar with material microdefects. ASCE-ASME J Risk Uncertain Eng Syst B 2019; 5(3): 030908.

[29] Gurson AL. Continuum theory of ductile rupture by void nucleation and growth: Part I-Yield criteria and flow rules for porous ductile media. J Eng Mater Technol-Trans ASME 1977; 99 (1): 2-15.

[30] Tvergaard V, Needleman A. Analysis of the cup-cone fracture in a round tensile bar, Acta Metall 1984; 32 (1): 157-169.

[31] Pardoen T, Hutchinson JW. An extended model for void growth and coalescence. J Mech Phys Solids 2000; 48(12): 2467-2512.

[32] Teng B, Wang W, Xu Y. Ductile fracture prediction in aluminium alloy 5A06 sheet forming based on GTN damage model. Eng Fract Mech 2017; 186: 242-254.

[33] Dunn CG, Kogh EF. Comparison of dislocation densities of primary and secondary recrystallization grains of Si-Fe. Acta Metall 1957; 5(10): 548-554.

[34] Adachi H, Miyajima Y, Sato M, Tsuji N. Evaluation of dislocation density for 1100 aluminum with different grain size during tensile deformation by using in-situ X-ray diffraction technique. Mater Trans 2015; L-M2015803.

[35] Schonberg WP. Characterizing material states in orbital debris impacts. In *Space Environmental, Legal, and Safety Issues*. International Society for Optics and Photonics 1995; 2483: 31-40.

[36] Meyers MA. Dynamic behavior of materials. USA: John wiley & Sons; 1994.

[37] Sellars CM. Recrystallization of metals during hot deformation. Phil Trans Roy Soc Lon Ser A 1978; 288(1350): 147-158.